JASA ARTICLE

Measuring the radiation of sound sources with the radiation mode method: Towards realistic problems

Maryna Sanalatii,[1] Philippe Herzog,[2] Manuel Melon,[3,a)] Régine Guillermin,[4] and Jean-Christophe Le Roux[1]

[1]*Centre de Transfert de Technologie (CTTM), 20 Rue de Thalès de Milet, 72000 Le Mans Cedex 09, France*

[2]*ARTEAC-LAB, 29 Rue Saint Savournin, 13005 Marseille, France*

[3]*Laboratoire d'Acoustique de l'Université du Mans (LAUM), UMR 6613, Institut d'Acoustique—Graduate School (IA-GS), CNRS, 72000 Le Mans, France*

[4]*LMA-CNRS, 4 Impasse Nikola Tesla, 13013 Marseille, France*

ABSTRACT:

The measurement of the pressure field radiated by a sound source has many applications in the fields of noise control and loudspeaker system design. In this paper, the radiation mode method is used to measure the field radiated by a complex acoustic source whose surface impedance is arbitrary and does not correspond to the Neumann boundary condition used for the calculation of radiation modes. The most effective radiation modes are used as test functions to calculate a pressure expansion around the source under test, an expansion that matches the measured pressure at a limited number of points close to the source. This expansion is then used to calculate the radiated pressure at a greater distance at unmeasured locations. In a first step, numerical simulations are performed to evaluate the method's most influential parameters. Then, measurements are performed in a semi-anechoic room on two real sources of increasing complexity. Obtained results show that the radiation mode method allows an accurate evaluation of the pressure field radiated by the test object over a fairly wide frequency band (between 100 Hz and 2 kHz) even for complex sources. © *2024 Acoustical Society of America*. https://doi.org/10.1121/10.0025022

(Received 10 August 2023; revised 17 January 2024; accepted 7 February 2024; published online 1 March 2024)

[Editor: Michael J. White] Pages: 1641–1654

I. INTRODUCTION

Many of the standards for determining the sound power level of noise sources require measurements in controlled environments, such as reverberating rooms[1] and semi-anechoic or anechoic rooms.[2,3] Similarly, standards for the measurement of loudspeaker drivers or systems require such expensive facilities,[4] with the added need of a very wide frequency range.

Several alternatives have been proposed to avoid the burden and cost of using such large measurement facilities. For the determination of the sound power level of noise sources, measurements may involve acoustic intensity measurements instead of acoustic pressure measurements, as this allows canceling of most of the influence of the surrounding room.[5] For the measurement of loudspeaker frequency responses, alternative methods have also been proposed:[6] One of the most used combines near-field measurements and gated measurements.[7]

Indeed, in many practical cases (e.g., at early design stages or for troubleshooting unexpected noise radiation), it is more convenient and somewhat sufficient to use measurements performed in the vicinity of the tested source. This approach is also proposed in standards.[8]

In the scientific literature, numerous techniques using measurements performed close to the source body have been developed, one of the most studied being the near-field acoustic holography (NAH) method. Many NAH methods have been considered to identify vibro-acoustic interactions, involving inverse propagation from a measurement surface back to the source body. Early methods used "Fourier NAH," i.e., expansion over the function basis associated with the separable coordinate system:[9–14] such methods are thus limited to compatible body geometries. Backward propagation between the measurement surface and a source body of arbitrary shape has been studied with numerical techniques, such as the inverse boundary element method (iBEM).[15–19] In such approaches, numerous measurements are required as the boundary element method (BEM) mesh must involve element sizes related to the highest frequency of interest.

Both the Fourier NAH method and iBEM require inversion of an ill-conditioned propagation matrix, because the evanescent components of the radiated field tend to vanish between the source body and the measurement surface. Regularization techniques are thus required, especially when backward-propagating noisy measurements. An alternative is to reduce the rank of the problem, e.g., by using coarser models, such as the inverse patch transfer function method (iPTF),[20] equivalent source method (ESM),[21] or the Helmholtz least squares (HELS) method.[22–25]

Moreover, measurements performed in non-anechoic rooms are influenced by the field reflected from nearby

a)Email: manuel.melon@univ-lemans.fr

objects and walls, which is, in turn, diffracted by the source body. Several techniques have been developed to cope with such situations: e.g., using two layers of measurements as in the field separation method (FSM) and other derived methods.[26–31]

A common property of the above techniques is that they aim at reconstructing the vibration field over the source body, thus requiring a backward propagation processing. As previously stated, this leads to a problematic matrix inversion requiring tricky regularization, with a great sensitivity to measurement noise and parasitic field components. Fortunately, many applications do not require a precise knowledge of the velocity field over the source body. Thus, the calculation of the radiated power or directivity patterns of the source under study can be obtained by forward propagating the measurement data. This is generally an easier problem because it deals with sound pressure radiated in the far field, which is much simpler to assess. This problem was solved by using ESM to reconstruct the radiated far field (e.g., for submarines) and draw directivity maps.[32,33]

The approach proposed in this paper also focuses on the forward propagation of measurements close to the source body. It is based on a proper orthogonal decomposition of the radiated field, thus reducing the number of independent components needed to describe it. This leads to a well-conditioned problem and allows using a limited number of pressure measurements. This paper takes up a method for characterizing sound sources proposed by the same authors, which was simulated from measurements on a power transformer with complex vibration patterns[34] and used for the measurements of loudspeaker systems in an anechoic room[35] and *in situ*.[36] This method was then assessed for various loudspeakers, including a tall line array system with a complex shape[37] for which simulations allowed study of the influence of identification distance, noise measurement, and number of expansion terms. All the previous studies, however, dealt with objects having rigid boundaries. The present paper thus focuses on sources featuring wall boundary conditions (BCs) differing from those used for the calculation of the radiation modes (RMs). The effect of reducing the size of the mesh used for the RM calculation is also investigated. The work presented here therefore aims to go beyond overly academic problems to address sources that are more typical of those encountered in industry.

The principle of the RM method is presented in Sec. II. Simulations are then provided in Sec. III, in the case of a complex object involving various BCs. These simulations also allow assessment of the influence of the main parameters of the method. Section IV then presents measurements performed on a mock-up of a similarly complex (but different) object, showing the robustness of the method. These results are then summarized and discussed in Sec. V.

II. PRESSURE RECONSTRUCTION USING THE RM METHOD

The basic idea behind the RM method is to expand the field radiated by a source with an arbitrary body shape over a series of terms corresponding to independent radiation problems. This series is determined from the radiation impedance corresponding to the specific body shape considered, hence leading to a proper orthogonal decomposition of the radiated field.

This technique is inspired by the works of Veronesi and Maynard,[16] who computed the radiated acoustic field with an inverse acoustic imaging technique (iBEM-NAH) regularized by a singular value decomposition (SVD), and of Borgiotti,[38] for which the radiated field of a vibrating body was expanded using the SVD decomposition of the propagating operator between the surface velocity of the body and some points in the exterior domain (acoustic transfer impedance). Later, Sarkissian[39] proposed to define the radiation operator on the surface of the vibrating body (acoustic surface impedance) and to use only its real part, associated with the far-field radiation.

The basic concept behind the RM method is thus the same as the iBEM technique. It has been mainly used for reconstructing the source surface velocities from near-field pressure measurements, a virtual backward propagation that amplifies evanescent components in the near field and thus requires a regularization technique to avoid noise amplification. Regularization is often based on SVD expansion with a suitable selection of terms, such as series truncation,[17] wave-vector filtering,[40] or the use of sparse methods.[18] Conversely, the forward propagation involved in estimating the far-field from the near-field benefits from the natural decrease in evanescent modes, and thus does not require a regularization technique—although it is beneficial to keep a minimum number of terms to reduce the number of measurements performed in the vicinity of the tested source. This application has also been described previously for measuring power transformers[34] and later for assessing the directivity of an audio "line array";[37] it is recalled here with further details.

A. Integral formulation

The radiation impedance provides a relation between the velocity and the pressure over the object surface. To compute it, we consider an arbitrary velocity distribution over the body and calculate the resulting pressure.

The pressure $p(\mathbf{r})$, radiated by a vibrating source of surface S at a point $\mathbf{r}$ in the volume V exterior to the vibrating body, is governed in the frequency domain by the Helmholtz equation,[41]

$$\nabla^2 p(\mathbf{r}) + k^2 p(\mathbf{r}) = 0, \tag{1}$$

where ∇^2 is the Laplace operator and $k = \omega/c$ is the wave number for angular frequency ω and sound celerity c.

We assume that the radiation impedance characterizes the exterior problem and does not need to take into account the vibratory behavior of the source. The surface S of the radiating body is thus supposed to be perfectly rigid, so that it can be described by an inhomogeneous Neumann BC, considering an $e^{+j\omega t}$ time convention,[41]

https://doi.org/10.1121/10.0025022

$$\frac{\partial p(\mathbf{r_s})}{\partial \mathbf{n}} = -j\omega\rho V_n(\mathbf{r_s}), \tag{2}$$

with ρ the air density, V_n the boundary normal velocity, $\mathbf{r_s}$ a point on the surface S of the radiating object, and $\mathbf{n}$ the normal oriented towards the exterior side of surface S.

Using the Green's function given in Eq. (3),

$$G(\mathbf{r}, \mathbf{r_s}) = \frac{1}{4\pi}\frac{e^{-jk|\mathbf{r}-\mathbf{r_s}|}}{|\mathbf{r}-\mathbf{r_s}|}, \tag{3}$$

the differential in Eq. (1) governing the solution in the whole domain and the BC in Eq. (2) can be combined into the integral, Eq. (4), over the boundary surface S,[42]

$$\alpha(\mathbf{r})p(\mathbf{r}) = \int_S \left(\frac{\partial G}{\partial \mathbf{n}}(\mathbf{r}, \mathbf{r_s})p(\mathbf{r_s}) + j\omega\rho G(\mathbf{r}, \mathbf{r_s})V_n(\mathbf{r_s})\right)dS, \tag{4}$$

where $\alpha(\mathbf{r}) = 1 + (1/4\pi)\int_S(\partial/\partial\mathbf{n})(1/|\mathbf{r}-\mathbf{r_s}|)dS$ is a geometric coefficient assigned to the solid angle seen from the point $\mathbf{r}$. It is equal to 1 for $\mathbf{r} \in V$ and to 1/2 for $\mathbf{r} \in S$.[43] This last equation, when applied to points on the surface S, leads to an integral equation relating $p(\mathbf{r_s})$ and $V_n(\mathbf{r_s})$.

B. RM calculation

For locations $\mathbf{r_s}$ belonging to S, the integral in Eq. (4) does not have a closed-form solution but can be solved numerically by discretizing the boundary S with a mesh of elements S_i, the size of which is small compared to the wavelengths of interest. Assuming constant pressure and volume velocity over each element, Eq. (4) may be transformed into the matrix form given by Eq. (5),

$$\frac{1}{2}\mathbf{p_s} = \mathbf{M}\mathbf{q_s} - \mathbf{D}\mathbf{p_s}, \tag{5}$$

where $\mathbf{p_s}$ and $\mathbf{q_s}$ are vectors of mean surface pressure and volume velocity over each element, respectively, and matrices $\mathbf{M}$ and $\mathbf{D}$ are filled from the two terms of the integral in Eq. (4):

$$\mathbf{M_{ij}} = j\omega\rho/S_i\int_{S_i} G(\mathbf{r_j}, \mathbf{r_i})dS(\mathbf{r_i}), \tag{6}$$

$$\mathbf{D_{ij}} = -\int_{S_i}\frac{\partial G}{\partial \mathbf{n}}(\mathbf{r_j}, \mathbf{r_i})dS(\mathbf{r_i}). \tag{7}$$

Equation (5) then allows computation of the relation between $\mathbf{p_s}$ and $\mathbf{q_s}$ as an impedance matrix, $\mathbf{Z}$, defined as $\mathbf{p_s} = \mathbf{Z}\,\mathbf{q_s}$, so

$$\mathbf{Z} = \left[\frac{1}{2}\mathbf{I} + \mathbf{D}\right]^{-1}\mathbf{M}. \tag{8}$$

Note that Eq. (8) does not depend on $\mathbf{p_s}$ or $\mathbf{q_s}$: it is the same, whatever source vibration pattern is considered. It can thus be used with any (unknown) $\mathbf{q_s}$ distribution to be identified.

As boundaries are considered to be perfectly rigid, the interior and exterior problems are independent, which simplifies the calculation of the far-field pressure. It has been stated that the real part of the impedance matrix represents the active part of the acoustic field (radiation in the far-field) and the imaginary part—the reactive part (evanescent field, close to the source body).[44,45]

The SVD of the $\mathbf{Z}$ matrix leads to independent solutions of the radiation problem,[46] which are called RMs in the remaining part of this paper.[34,37] As we are interested in the far-field radiation, only the real part of the impedance matrix is expanded,[39]

$$\Re(\mathbf{Z}) = \mathbf{U}\mathbf{\Sigma}\mathbf{V}^*, \tag{9}$$

where $\mathbf{U}$ and $\mathbf{V}$ contain sets of vectors corresponding to pressure and volume velocity of each element, respectively, $\mathbf{\Sigma}$ is a square diagonal matrix with positive real values representing the relative efficiency of each term, and the superscript symbol * denotes the conjugate transpose.

Expressed in this way, RMs (columns of $\mathbf{V}$ matrix) constitute a set of orthogonal functions over the surface S. They therefore allow expansion of the volume velocity over the source body, as proposed by Bi *et al.*[18] Here, we however focus on the far-field estimation, so the series is truncated in order to keep only the most efficient radiating RMs. The far-field pressure is approximated by the linear combination of a limited number, N, of RMs with appropriate weighting coefficients $\mathbf{w}$.

The pressure radiated by each RM may then be propagated independently at any location in the exterior domain using a discretized version of Eq. (4), which has a closed-form solution for locations at sufficient distance from S. Considering such a set of locations, the corresponding pressures $\mathbf{p}$ may be expressed as

$$\mathbf{p} = \mathbf{H}\mathbf{w}, \tag{10}$$

where $\mathbf{H}$ is a matrix for which columns are the pressures radiated by the RMs at the considered locations. This propagation matrix depends on the source geometry and on the considered locations, but not on the vibration pattern over the source surface. It may be computed using a standard BEM code, when RMs have been determined.

C. RM weighting

The weighting coefficients $\mathbf{w}$ may be identified from actual pressure measurements $\mathbf{p_i}$ performed in the vicinity of the tested source, at the so-called identification positions P_i. Indeed, the radiated field expansion approximates the field at any location, so the coefficients estimated at the P_i should be valid at other locations.

Using the pseudo-inverse of the transfer matrix $\mathbf{H_i}$ between RM volume velocities $\mathbf{V}$ and resulting pressure at P_i, computed with Eq. (4), the vector $\mathbf{w}$ can be expressed as follows:

$$\mathbf{w} = (\mathbf{H}_\mathbf{i}^* \mathbf{H}_\mathbf{i})^{-1} \mathbf{H}_\mathbf{i}^* \mathbf{p}_\mathbf{i}. \tag{11}$$

Although the RMs correspond to independent radiation problems, unsuitable choice of the identification point locations might lead to redundant ones. In this case, Eq. (11) would represent an ill-posed problem, requiring regularization. The number of the identification pressure measurements $\mathbf{p_i}$ is therefore chosen slightly larger than the number of RMs: We use 25% more identification points than the number of RMs. This also improves the robustness to measurement noise.

The number of RMs is defined from the RM efficiency matrix $\mathbf{\Sigma}$, as reported in Ref. 37. The set of RMs is truncated to the N most efficient ones, with no other selection criterion than their radiation efficiency.

The choice of P_i locations results from a trade-off between being close enough to ensure a good signal-to-noise ratio (SNR) and being far enough so that the evanescent pressure field does not dominate.[37]

D. Pressure estimation

Assuming the RM weighting coefficients are valid over all the far-field part of V, the pressure $\mathbf{p_e}$ may now be estimated at all interesting locations P_e in the far-field,

$$\mathbf{p_e} = \mathbf{H_e w}, \tag{12}$$

where $\mathbf{H_e}$ is the matrix of transfer functions between the RMs and the estimation points P_e; it is computed numerically similarly to $\mathbf{H_i}$.

III. SIMULATIONS

The objective of the present paper is to validate the RM method for realistic problems and especially for objects with various BCs. As complex geometries have already been studied,[34,37] we chose a simple one compatible with both simulations and measurements.

Figure 1 shows this geometry: the gray rectangular parallelepiped with extreme corners at $[x_1 = 0, y_1 = 0, z_1 = 0]$ m and $[x_2 = 0.50, y_2 = 0.40, z_2 = 0.665]$ m represents the acoustic source of interest, radiating above a rigid ground located at $z_g = -0.8$ m. The grid of 380 identification points (P_i) is shown in light gray, and the distance between the closest points of the grid is 0.12 or 0.13 m, depending on the direction. All planes of P_i are parallels to one side of the source and are placed 20 cm away from it. Three planes, XY, XZ, and YZ, with, respectively, 48, 42, and 48 estimation points (P_e) are shown by thick black points. They are located 0.80 m above the source (XY) or 0.50 m (XZ) and 0.90 m (YZ) away from two sides of the source. The distance between two nearest points of each plane is about 0.20 m. The lowest P_e are located at 0.07 m from the ground. Dimensions of the three P_e planes are given in Table I. An additional set of P_e, represented by thin black points, is a hemisphere with a radius of 3 m and composed of 694 points, which will be used in Sec. III D.

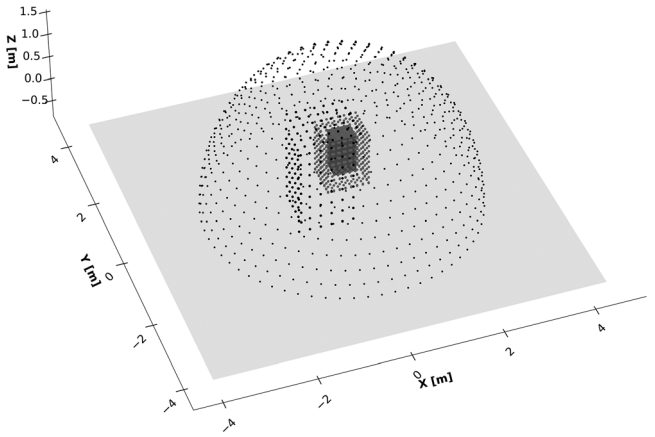

FIG. 1. Problem geometry. The gray rectangular parallelepiped represents the radiating source. The light gray rectangular surface corresponds to an infinite reflecting plane located at $z_g = -0.8$ m. The light gray points show 380 identification points (P_i), the thick black points show three planes of 138 estimated points (P_e), and thin black points represent a hemisphere of 694 additional P_e.

Each of the 6 sides of the simulated source contains circular zones to which a vibration pattern and/or admittance BC can be applied. The frequency dependence of the velocity functions is defined as 2nd order bandpass filters centered on a specific frequency, f_0. The filter complex amplitude is given by $V(f) = (jV_0/Qf/f_0)/(1 - f^2/f_0^2 + jf/f_0Q)$, where f is the frequency and $Q = 8$ is the filter quality factor. This permits highlighting a clearly visible peak at the central frequency f_0. The exploded view of the tested source is given in Fig. 2, while the characteristics of the different zones are summarized in Table II.

The vibrating parts have a uniform velocity with a maximum amplitude of $V_0 = 1$ m/s at f_0 for sets 1, 6, and 7 (cf. Table II). The velocity of sets 2 and 3 is weighted by a coefficient leading to the same maximal volume velocity as for sets 1, 6, and 7.

Zones with admittance use the same frequency dependence function, $A(f) = (jA_0/Qf/f_0)/(1 - f^2/f_0^2 + jf/f_0Q)$, with an amplitude of $A_0 = 1/\rho c$ m^{2}s/kg at f_0, air density $\rho = 1.204$ kg/m^3, and sound celerity $c = 343$ m/s. This value may seem somewhat extreme, but it allows us to move away enough from the Neumann (rigid wall) BCs used for the RM calculation.

Set 10 of Table II contains the source parts, which were not mentioned in the previous non-overlapping sets (1 to 9). Thus, the union of the ten sets builds the complete closed parallelepipedic source surface.

Three source configurations of increasing complexity were constructed from the vibration patterns and admittance values provided in Table II:

(1) V1A0. Only one disk (set 1 of Table II), with admittance $A(f)$, is vibrating on the top of the perfectly rigid body. The admittance of sets 2 to 10 corresponds to a rigid case scenario ($A = 0$).
(2) VTAT. All vibrating disks and zones with admittance $A(f)$ are "turned on" (sets 1 to 9 from Table II). Set 10 is considered to be perfectly rigid ($A = 0$).

https://doi.org/10.1121/10.0025022

TABLE I. Dimensions of the three planes of estimation points (P_e).

Set	Plane	Extreme corners
1	XY	$[-0.95, -0.90, 1.465]$ m and $[0.25, 0.20, 1.465]$ m
2	XZ	$[-0.95, -0.50, -0.70]$ m and $[0.25, 0.50, 1.00]$ m
3	YZ	$[-0.90, -0.50, -0.50]$ m and $[-0.90, 0.40, 1.00]$ m

(3) RABS. All vibrating disks and zones with admittance $A(f)$ are "turned on" (sets 1 to 9 from Table II). Set 10 has a constant admittance $A = 1/\rho c$.

Case V1A0 has then almost the same boundary Neumann conditions as those used for the RM computations (however, with a source admittance and a different mesh). This is a reference case, similar to the ones considered in previous studies.[18,34,37] Case VTAT has a much greater complexity, with various vibration patterns and admittance conditions that are not taken into account for RM computations. It is a realistic case, similar to the experimental one considered in Sec. IV. The RABS case considers an absorbing condition on all rigid surfaces of case VTAT: although not a realistic configuration, it is interesting as an extreme situation for which the entire surface of the system has BCs different from the model used for RM computations.

Note that, for a band-pass volume velocity frequency dependence, the radiated pressure has a high-pass behaviour. Thus, for configurations VTAT and RABS, the number of active radiating surfaces increases with frequency, and five sources (sets 1 to 3, 6, and 7 from Table II) of equal volume acceleration are radiating in the upper frequency band.

The acoustic pressure at P_i and P_e for the three source configurations V1A0, VTAT, and RABS is computed using the commercial software SYSNOISE (using the BEM). The source is discretized with elements having an average length of 17 mm, leading to results accurate up to 3 kHz according to the common criterion of at least 6 mesh elements per wavelength. A reflecting plane is set at $z_g = -0.8$ m.

RMs are computed with a custom BEM code named FELIN, developed at Laboratoire de Mécanique et d'Acoustique (LMA) using published integration routines.[47] This RM computation is based on a mesh with elements of 28 mm average side length and considers the Neumann BC on the entire surface of the source and a reflecting plane at $z_g = -0.8$ m.

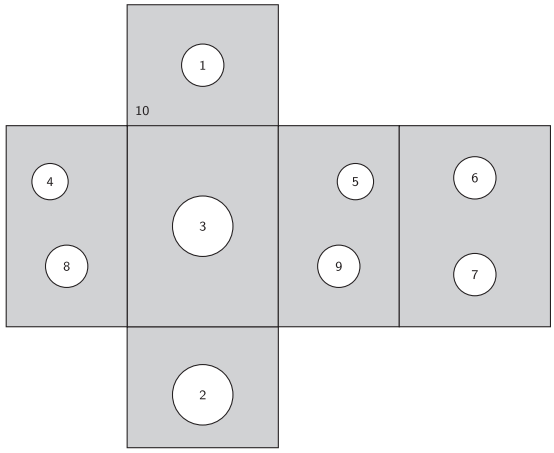

FIG. 2. Exploded view of the tested source highlighting the different zones; their characteristics are given in Table II.

Results are studied in the 30 Hz to 2 kHz frequency band. The upper frequency results from the mesh size of the BEM model. The lower frequency has been arbitrarily chosen because, at lower frequencies, most actual sources have a low efficiency, which does not allow them to reach a good SNR.

As expressed, the RM method is based on "radiating RMs" determined from the real part of the radiation impedance. However, it was shown in Ref. 37 that even if some evanescent field is present at the P_i locations (which is barely avoidable at lower frequencies), a correct far-field reconstruction is possible. We assume this is still the case for the present paper, although this aspect would need further investigations.

Pressure reconstruction is performed using the N_m most efficient modes, with a slight difference compared to previous work: N_m is first chosen for 90% total efficiency according to the $\mathbf{\Sigma}$ efficiency matrix, and 20 more RMs are then added to the first N_m ones, as this ensures a minimum number of terms at lower frequencies. This results in an even reconstruction accuracy over the whole frequency band.

Actual measurements are always affected by the presence of electrical and acoustic noise. Thus, in order to bring

TABLE II. Radiating source BCs.

Set	Frequency band	Central frequency	Face	Center	Radius	Vibration	Admittance
1	31 − 62 Hz	$f_0 = 44$ Hz	$z = z_2$	$[x_2/2,\ y_2/2,\ z_2]$ m	0.07 m	$V(f, f_0)$	$A(f, f_0)$
2	62 − 125 Hz	$f_0 = 88$ Hz	$z = z_1$	$[x_2/2,\ y_2/2,\ z_1]$ m	0.10 m	$V(f, f_0)$	$A(f, f_0)$ or 0
3	125 − 250 Hz	$f_0 = 177$ Hz	$y = y_1$	$[x_2/2,\ y_1,\ z_2/2]$ m	0.10 m	$V(f, f_0)$	$A(f, f_0)$ or 0
4	250 − 500 Hz	$f_0 = 354$ Hz	$x = x_1$	$[x_1,\ y_3 = 0.255, z_3 = 0.480]$ m	0.06 m	0	$A(f, f_0)$ or 0
5	250 − 500 Hz	$f_0 = 354$ Hz	$x = x_2$	$[x_2,\ y_3 = 0.255, z_3 = 0.480]$ m	0.06 m	0	$A(f, f_0)$ or 0
6	0.5–1 kHz	$f_0 = 707$ Hz	$y = y_2$	$[x_2/2,\ y_1, z_2/2 + 0.16]$ m	0.07 m	$V(f, f_0)$	$A(f, f_0)$ or 0
7	0.5–1 kHz	$f_0 = 707$ Hz	$y = y_2$	$[x_2/2,\ y_1, z_2/2 - 0.16]$ m	0.07 m	$V(f, f_0)$	$A(f, f_0)$ or 0
8	1 − 2 kHz	$f_0 = 1414$ Hz	$x = x_1$	$[x_1,\ y_2/2, z_4 = 0.20]$ m	0.07 m	0	$A(f, f_0)$ or 0
9	1 − 2 kHz	$f_0 = 1414$ Hz	$x = x_2$	$[x_2,\ y_2/2, z_4 = 0.20]$ m	0.07 m	0	$A(f, f_0)$ or 0
10	31 Hz −2 kHz	N/A[a]	All	N/A	N/A	0	0 or $1/\rho c$

[a]N/A, not applicable.

the simulation conditions closer to the experimental ones, the pressures at the P_i were blurred using additive noise. The amplitude of the noise is set to be 40 dB lower than the mean pressure at the P_i, while its phase is a random function with a uniform distribution over $[0, 2\pi]$. This choice leads to an error between 0 and 0.1 dB at the P_i. No noise has been added to the P_e because we want here to assess the reproduction error.

For the three source configurations, Fig. 3 compares the radiated pressure computed with a BEM and the pressure reconstructed using the RM method at point $[-0.9, -0.505, 0.37]$ m.

The pressure reconstruction is rather accurate: The difference in pressure level between RM reconstruction and simulation is less than 1 dB over almost the whole frequency band from 30 Hz to 1 kHz and less than 2 dB up to 2 kHz. The difference mostly rises at the pressure level dips, where the RMs are less efficient and the SNR lower. This is characteristic of the RM method, for which the most efficient modes were chosen, thus favoring directions where the radiated pressure is high.

It is remarkable that an expansion using RMs computed with Neumann BCs is able to represent radiating objects with quite different ones—especially case RABS, which has no surface respecting the Neumann BC. It may only be remarked that the pressure reconstruction of the V1A0 configuration has a slightly better accuracy than the two other setups over all the frequency range, which may be related to the fact that this simpler source has a smoother frequency response.

The results presented in Fig. 3 therefore tend to indicate that the RM series is valid for both any vibration shape and for any BC over the source body. This is quite interesting for practical purposes, as it would be difficult to know BCs in actual situations.

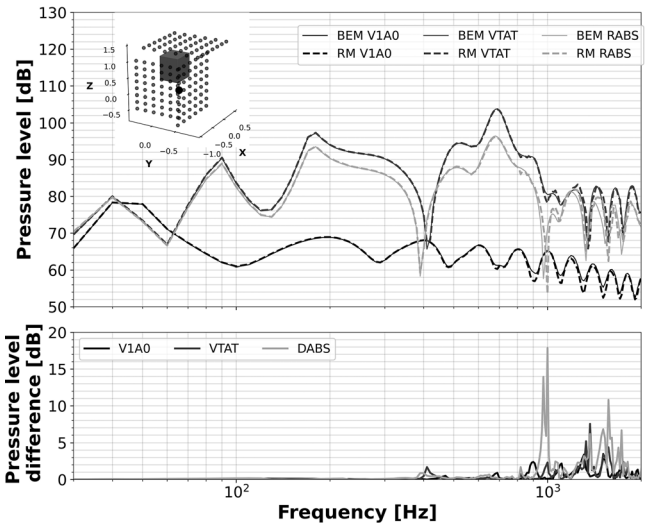

FIG. 3. (Upper graph) Frequency response of configurations V1A0, VTAT, and RABS at the point depicted by •: BEM computation and RM reconstruction. (Lower graph) The pressure level difference between BEM computation and RM reconstruction.

The normalized reproduction error E_r calculated over all P_e is given by Eq. (13) and is shown in the upper part of Fig. 4,

$$E_r = 10\log_{10}\left(\frac{(\mathbf{p_{rm}} - \mathbf{p_r})^*(\mathbf{p_{rm}} - \mathbf{p_r})}{\mathbf{p}^*_{\mathbf{rm}}\mathbf{p_{rm}}}\right), \tag{13}$$

where $\mathbf{p_{rm}}$ is the vector of pressures estimated by the RM technique and $\mathbf{p_r}$ is the vector of pressures computed using the BEM software.

The following simulations deal with the effect of the main parameters of the RM method. These simulations are performed for the VTAT case, which is the most realistic configuration among those proposed. Note that the following simulations are still using noisy pressures for P_i but not for P_e.

A. Number of identification points (P_i)

Previous pressure estimations were realized using a grid of 380 regularly spaced P_i, which would be very time consuming in practice. A more realistic number of P_i has been searched, considering the six following configurations of P_i shown in Fig. 5:

- G consists of a grid of 380 points creating a rectangular parallelepiped with extreme corners located at $[x = x_1 - 0.2, y = y_1 - 0.2, z = z_1 - 0.2]$ m and $[x = x_2 + 0.2, y = y_2 + 0.2, z = z_2 + 0.2]$ m; thus, all P_i are 20 cm away from each side of the source [see Fig. 5(a)]. G is the grid used for the simulations presented so far.
- G/4 consists of a grid of 95 points [see Fig. 5(b)].
- G/6 consists of a grid of 64 points [see Fig. 5(c)].
- G/8 consists of a grid of 48 points [see Fig. 5(d)].
- G/12 consists of a grid of 32 points [see Fig. 5(e)].
- G/24 consists of a grid of 16 points [see Fig. 5(f)].

The P_i for grids G/4, G/6, G/8, G/12, and G/24 were randomly chosen from grid G in order to ensure an almost homogeneous distribution around the source.

As stated above, we ensure an overdetermination when computing the pseudo-inverse of the transfer matrix $\mathbf{H_i}$. The number of used RMs has therefore been limited to 80%

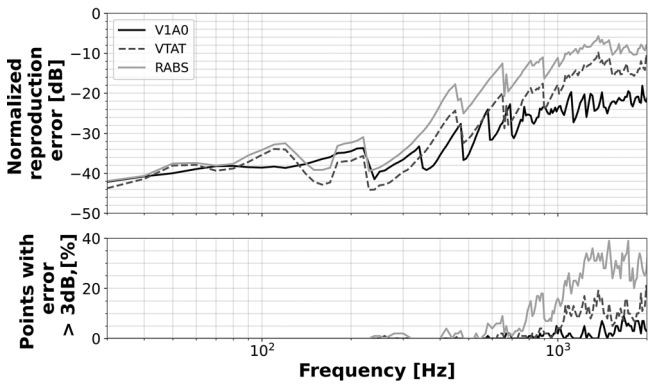

FIG. 4. (Upper graph) Global reproduction error E_r for the configurations V1A0, VTAT, and RABS. (Lower graph) Percentage of points with error higher than 3 dB.

https://doi.org/10.1121/10.0025022

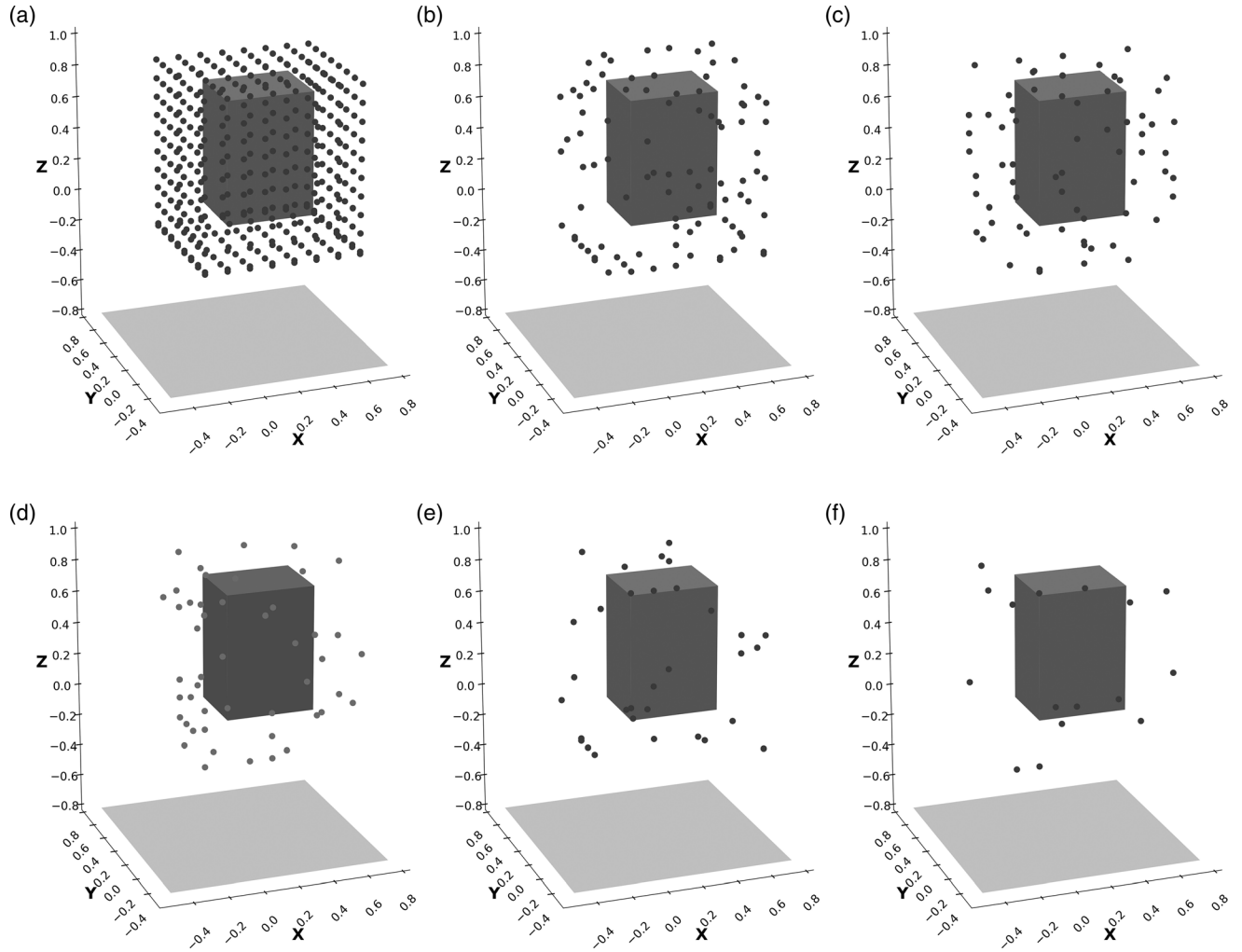

FIG. 5. Six grids of identification points P_i: G (a), G/4 (b), G/6 (c), G/8 (d), G/12 (e), and G/24 (f).

of the number of P_i for each tested grid. This can be seen on Fig. 6, where the RM number is almost constant at lower frequencies, rising slowly over the minimum value of 20. The quicker rise at mid frequencies is governed by the RM radiation efficiencies, while the number at higher frequencies is limited by the selected number of P_i.

The global reproduction error and the pressure estimation at one point are presented in Figs. 7 and 8, respectively. It can be noticed that meshes G/12 and G/24 exhibit a larger error than the other meshes at low frequencies. Also, a sharp error increase occurs above frequencies for which the maximum number of RMs is reached. This limit might be overcome by using more RMs at higher frequencies, thus requiring regularization of the underdetermined problem, or by a different selection of the RMs. Another solution would be to implement a sparse regularization method as proposed by Bi *et al.*[18] This improvement is however beyond the scope of the present work.

B. Discretization of the radiating surfaces

A common rule of thumb of 6 elements per wavelength is usually used to define a mesh size (element's side length). However this rule might be somewhat relaxed for the RM computation, as mentioned in previous papers.[36,37] In this section, we thus compare the results estimated from RMs computed using coarser meshes with element sizes larger than the one used until now ($D = 28$ mm): i.e., $D = 70$, 112, 224, and 448 mm. All computations are done with a grid G

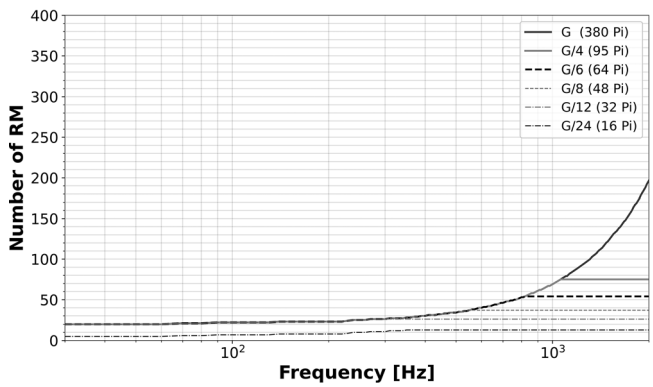

FIG. 6. Number of RMs used for estimation with six grids of P_i (G, G/4, G/6, G/8, G/12, and G/24).

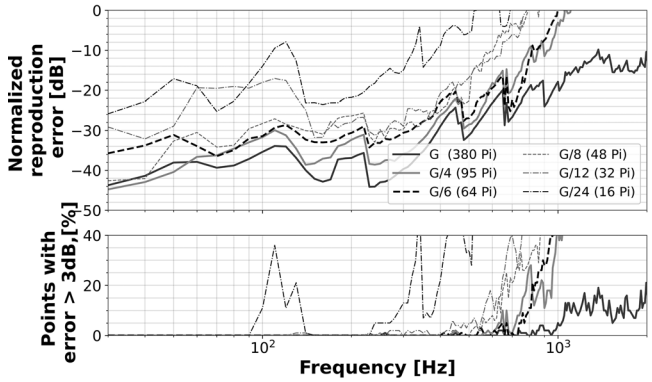

FIG. 7. (Upper graph) Global reproduction error E_r for G, G/4, G/6, G/8, G/12, and G/24. (Lower graph) Percentage of points with an inaccuracy larger than 3 dB.

of 380 P_i. Details concerning the five tested meshes used here are given in Table III, and results are plotted in Fig. 9.

This figure shows that the mesh might be coarsened up to about 1 element per wavelength. This probably results from the fact that we are using only the first RMs, which usually have simple shapes, and may thus be described by a coarser mesh than the actual vibration shapes. Selection of higher order ones might lead to different requirements. In our case, such a coarse mesh allows a tremendous decrease in the computation time: The time needed to compute and expand the impedance matrix decreases rapidly with the number of elements, itself decreasing with the mesh size. For coarser meshes, the overall computation time is thus dominated by the one related to propagating the RM patterns toward the field points. Therefore, since a dense frequency vector is required in the experimental part of the paper (Sec. IV), we use a 70 mm mesh size, which provides almost the same result as a 28 mm mesh size up to 2 kHz but reduces the computation time by a factor of around 80.

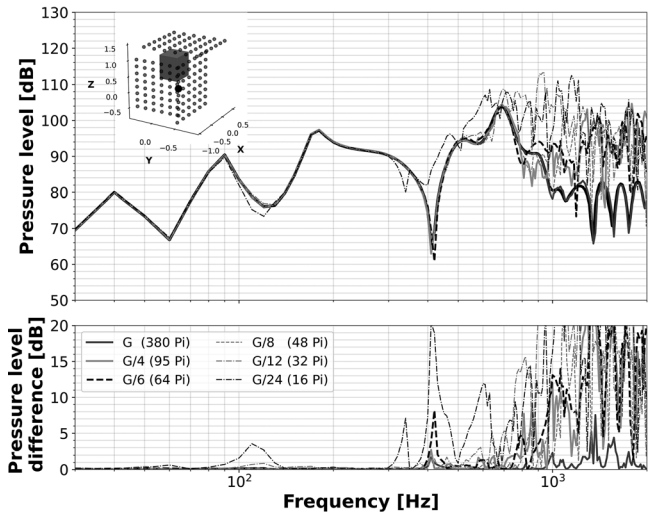

FIG. 8. (Upper graph) RM frequency response reconstruction with grids G, G/4, G/6, G/8, G/12, and G/24 at the point depicted by •. (Lower graph) The pressure level difference between reconstruction with the grid G and grids G/4, G/6, G/8, and G/12.

TABLE III. Computation details.

Parameter	Result for mesh element length of: 28 mm	70 mm	112 mm	224 mm	448 mm
No. of elements in the mesh	5620	978	440	160	56
No. of computed RMs	200	200	200	160	56
No. of points	1388	1388	1388	1388	1388
No. of computed frequencies	158	158	158	158	158
Computation time[a]	54 h	38 min	17 min	3.5 min	55 s

[a]Using a Xeon processor (4 cores) running at 3.6 GHz.

C. Bringing simulation closer to measurements

The noise added at P_i allows to evaluate the robustness of the RM method, but such simulation does not allow us to anticipate the performance of the RM results in the subsequent experiments presented in Sec. IV, for which pressures at P_i and P_e are both noisy. So, we also added noise at the P_e. The amplitude of this additive noise was set 40 dB lower than the mean pressure at the P_i, with a phase defined as a random function with a uniform distribution in $[0, 2\pi]$, leading to a 1 to 2 dB error at P_e.

Since both pressures at P_i and P_e are noisy, the difference between BEM computation and their estimation using the RM method should be considered as a "discrepancy" E'_r rather than an "error." This discrepancy is calculated using Eq. (14),

$$E'_r = 10\log_{10}\left(\frac{(\mathbf{p_{rm}} - \mathbf{p'^{*}_r})(\mathbf{p_{rm}} - \mathbf{p'_r})}{\mathbf{p^{*}_{rm}}\mathbf{p_{rm}}}\right), \tag{14}$$

where $\mathbf{p_{rm}}$ is the vector of the pressures estimated by the RM technique and $\mathbf{p'_r}$ is the vector of pressures computed with the BEM with additive noise. This equation will also be used in Sec. IV, where all measurements will inevitably be noisy.

The results are presented in Fig. 10. Due to the additive noise at both P_i and P_e, we can see a significant increase in the reconstruction discrepancy E'_r compared to the reconstruction error E_r. This is only noticeable at lower frequencies in our case and is hardly perceptible at higher

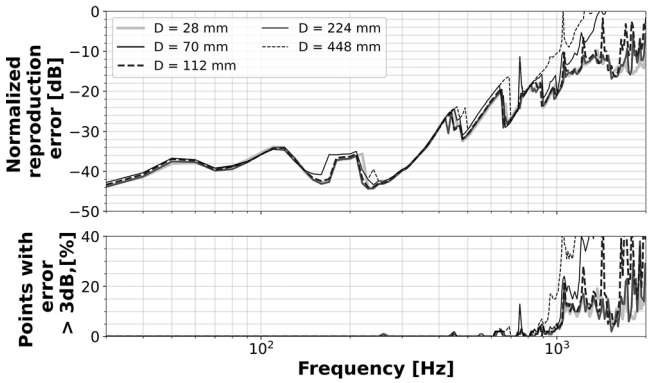

FIG. 9. (Upper graph) Global reproduction error E_r for mesh element size $D = 28$, 70, 112, 224, and 448 mm. (Lower graph) Percentage of points with an inaccuracy larger than 3 dB.

https://doi.org/10.1121/10.0025022

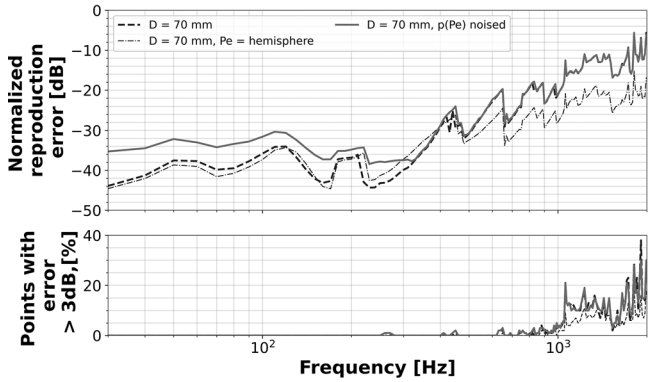

FIG. 10. (Upper graph) Global reproduction error E_r of the reconstructed pressure with additive noise at P_i only (light gray dashed curve), with additive noise at P_i and P_e (gray plain curve) and pressure reconstruction on points P_e located on the virtual hemisphere (light-gray dashed-dotted curve). (Lower graph) Percentage of points with an inaccuracy larger than 3 dB.

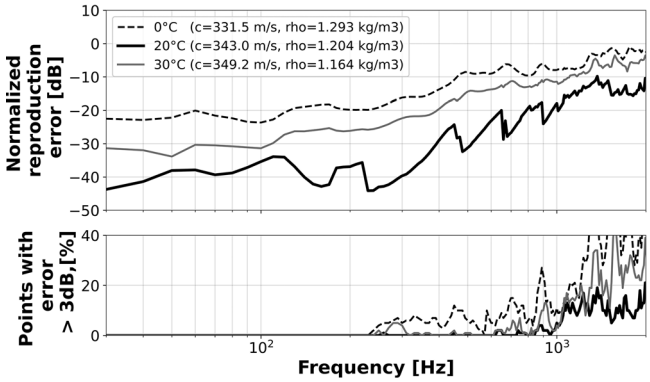

FIG. 11. (Upper graph) Global reproduction error for three temperatures for the VTAT configuration. (Lower graph) Percentage of points with an inaccuracy larger than 3 dB.

frequencies, where the reconstruction error is much larger when compared to the one due to the added noise.

D. Pressure reconstruction over a hemisphere

The RMs computed from the real part of the impedance matrix are better suited to represent the far-field pressure, as stated in Sec. II B. Therefore, P_e locations further away should lead to more accurate field reconstruction. This can be seen on Fig. 10, where a thin dashed-dotted line represents the normalized reproduction error for a hemisphere of 694 points located 3 m away from the source (small black points of Fig. 1). The RM method thus allows computation of pressures at intermediate distances, such as the one considered for the P_e planes, which are compatible with usual measurement facilities. However, it is even better suited to estimate the acoustic pressure at greater distances that can barely be considered for actual measurements. Moreover, a great number of far-field estimations may be obtained from a much smaller number of measurements close to the source. Anechoic measurements may even be estimated from *in situ* measurements.[36]

E. Effect of temperature

This section examines the effect of temperature variations on the pressure estimation using the RM technique. Virtual measurements on P_i were computed for large temperature variations: 0 °C ($c = 331.5$ m/s, $\rho = 1.293$ kg/m^3), 20 °C ($c = 343.0$ m/s, $\rho = 1.204$ kg/m^3), and 30 °C ($c = 349.2$ m/s, $\rho = 1.164$ kg/m^3). The goal is to reconstruct the pressure field at 20 °C using the RMs also computed at 20 °C.

Results are given in Fig. 11. One can note that the higher is the deviation from the VM temperature, the higher is the extrapolated pressure discrepancy. However, this discrepancy mostly increases at the dips of the pressure levels, as it can be seen in Fig. 12. Thus, the inevitable temperature variations when measuring pressure signals at the P_i (using a single moving microphone) should result in an acceptable discrepancy.

IV. MEASUREMENTS

In this section, the RM method is now assessed on actual acoustic sources. Two different systems have been built:

- Closed box source. A rigid box of outer dimensions $0.4 \times 0.5 \times 0.665$ m is equipped with a Scan-Speak 18S/8531G00 loudspeaker (Scan-Speak A/S, Videbaek, Denmark) of diameter 0.14 m, located on the top face [see Fig. 13(a)]. The enclosure is built with 20 mm thick medium density fiberwood (MDF) panels. Internal metallic bracing is added to strengthen the structure.
- Complex box source. The complex box source has the same structure as the closed box source, but with three important changes: a rectangular vent of 0.05×0.20 m has been added, connecting the interior volume to the exterior one. A 0.12 m diameter horizontal through tube is now connecting two sides of the source, and two facing wooden faces have been replaced by Plexiglas plates of

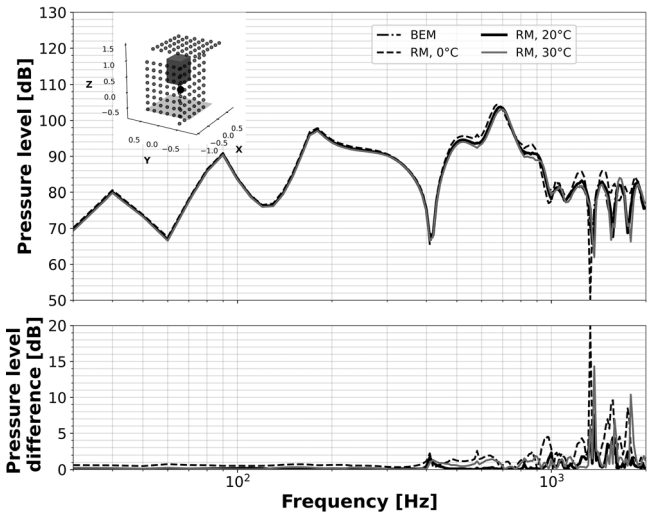

FIG. 12. (Upper graph) RM reconstruction of the frequency response with the temperature variation at the point depicted by •. (Lower graph) The pressure level difference between BEM calculation and RM reconstruction for 0 °C, 20 °C, and 30 °C.

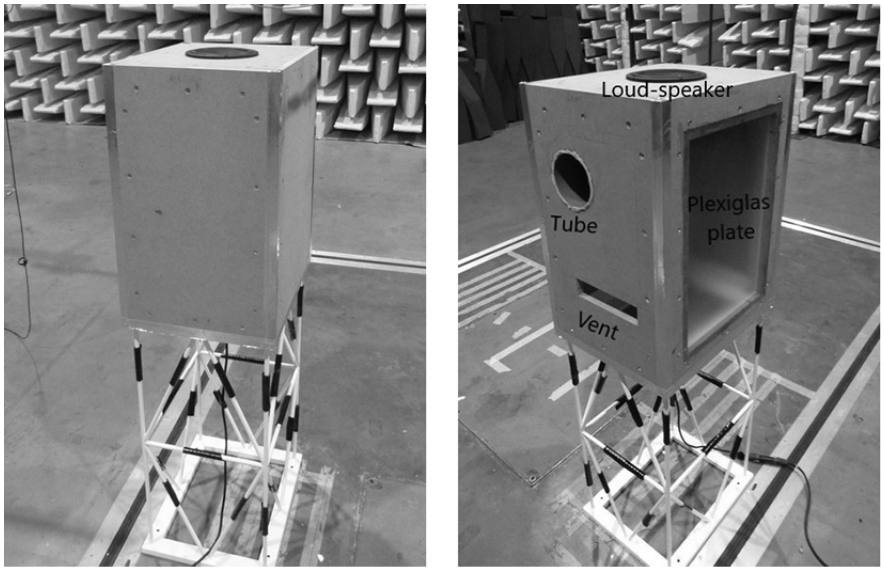

FIG. 13. Tested radiating sources: Closed box (a) and complex box with a 0.05 × 0.20 m rectangular vent, a 0.12 m diameter through tube, and 2 Plexiglas plates (b).

1 and 2 mm thickness [see Fig. 13(b)]. The intention behind this design is to create a source with complex BCs, significantly different from the Neumann conditions used for RM calculation, and with a complex acoustic radiation pattern.

For the measurements, each source was attached to the top of a 0.778 m high metallic structure, which consists of 12 mm diameter perforated tubes. Bitumen strips were attached to the tubes to dampen parasitic vibrations.

All measurements were carried out in the semi-anechoic room of Centre de Transfert de Technologie (CTTM), which has a working volume of 1000 m^3 and a cut-off frequency of 70 Hz. Pressure signals at P_i and P_e were recorded using a single 1/2 in. Brüel & Kjaer microphone connected to a Nexus conditioning amplifier (Brüel & Kjaer, Virum, Denmark). A National Instruments USB-4431 acquisition board was used for the acquisition (National Instruments, Austin, TX). The microphone was moved to each measurement position using a three-axis robot, thus avoiding calibration issues. Both sources were driven by an amplifier providing a 5 root mean square volt (Vrms) step sine signal from 42 Hz to 5 kHz with a 3 Hz frequency resolution.

The frequency transfer functions between amplifier input voltage (0.5 Vrms) and measured pressure were computed using from 5 to 20 steady-state measurement averages and from 12 to 60 settle cycles. The number of averages and settle cycles were adapted according to the output and input signals' coherence. Generation of the excitation signal, microphone signal acquisition, as well as results post-processing were carried out using INTAC, a measurement software developed at CTTM.

The 380 P_i are located as presented in case G from Sec. III A, and the P_e positions are the ones presented in Sec. III and Table I. The pressure calculation with the RM method is performed using a regular mesh with a 70 mm element size. As for the simulations, pressure reconstruction is computed with $N_m + 20$ RMs. The two tested sources were measured over a period of 2 weeks with temperature variations between 14 °C and 17 °C. Consequently, the RMs were calculated for a temperature of 15 °C ($c = 340$ m/s, $\rho = 1.225$

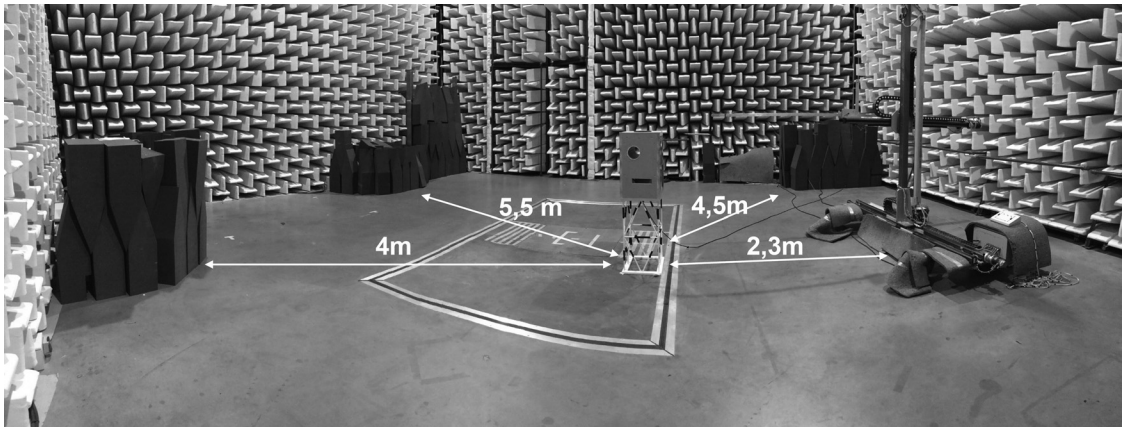

FIG. 14. Panoramic view of the measurement set-up with the "complex box" source.

https://doi.org/10.1121/10.0025022

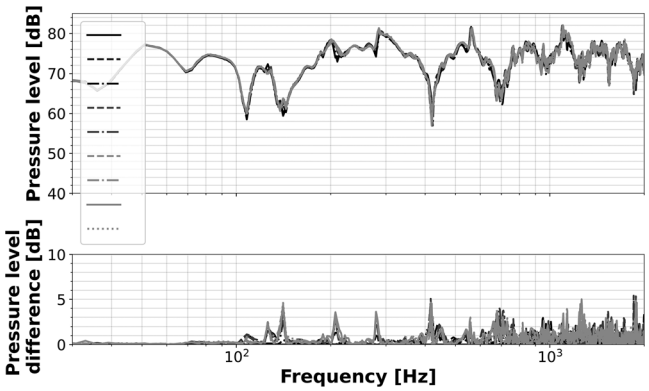

FIG. 15. Stability of the measurement system for the closed box source. (Upper graph) Nine measurements of the pressure level at the same position. (Lower graph) Pressure level differences.

kg/m^3). The panoramic view of the measurement set-up is presented in Fig. 14.

A second 1/2 in. Brüel & Kjaer microphone was placed at a fixed position about 4 m from the source. The purpose of this microphone was to monitor the stability of the source during the measurement campaign. Figures 15 and 16 show the stability of the set-up for the "closed box" and "complex box" sources, respectively. Nine measurements are plotted on each figure: The 5 first ones were taken during the measurements of P_i and the 4 last ones during the measurements of P_e. The measurements were carried out on various days, with different positions of the robot arm and with different room temperatures. This being said, the difference between the "control measurements" of the "closed box system," which is around ± 2 dB (see Fig. 15) at mid and high frequencies seems rather acceptable. On the other hand, the structure of the "complex box" source introduces much more disturbance of the radiated pressure field: an inaccuracy of about ± 3 dB can be noticed even at low frequencies, reaching as much as ± 6 dB for some frequencies. It is suspected that this instability in the response of the "complex" source is mainly due to the behavior of the Plexiglas plates, which evolved during the measurements and probably changed the BCs and the acoustic radiation.

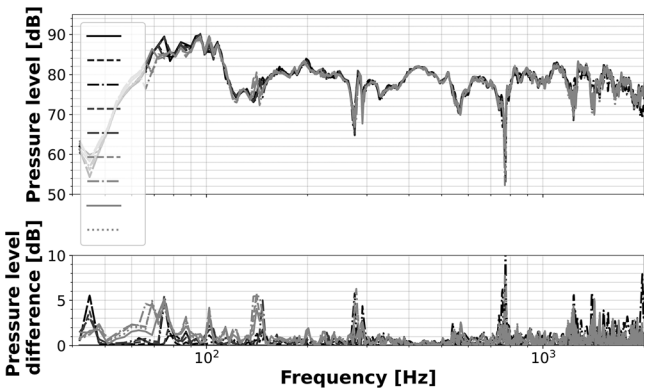

FIG. 16. Stability of the measurement system for the complex box source. (Upper graph) Nine measurements of the pressure level at the same position. (Lower graph) Pressure level differences.

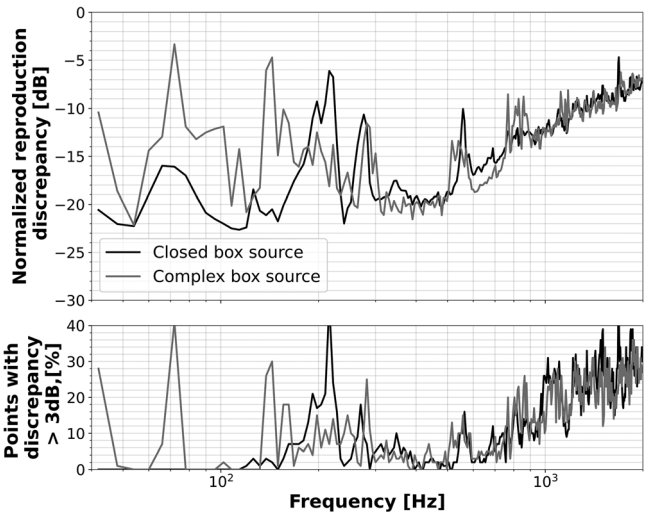

FIG. 17. (Upper graph) Global reproduction discrepancy of the pressure reconstruction of the "closed box" and "complex box" sources. (Lower graph) Percentage of points where a difference between pressure measurement and estimation is superior to 3 dB.

Figure 17 shows the global discrepancy of the RM pressure reconstruction for the "closed box" and "complex box" sources.

The fact that the discrepancy of the global reconstruction increases with frequency for the tested sources can be explained by 2 phenomena: (1) not optimal positions of P_i, where some of the points possibly provide a redundant information,[37] and (2) sharp local dips of pressure level, which are hardly reconstructed by RMs, which are selected for their radiation efficiency.

It can also be seen that the reconstruction discrepancy peaks for the "complex box" observed around 40, 70, 150, 280, 550, and 780 Hz coincide with the pressure level deviations due the system instability during measurements (see Fig. 16). A similar situation can be reported for the "closed

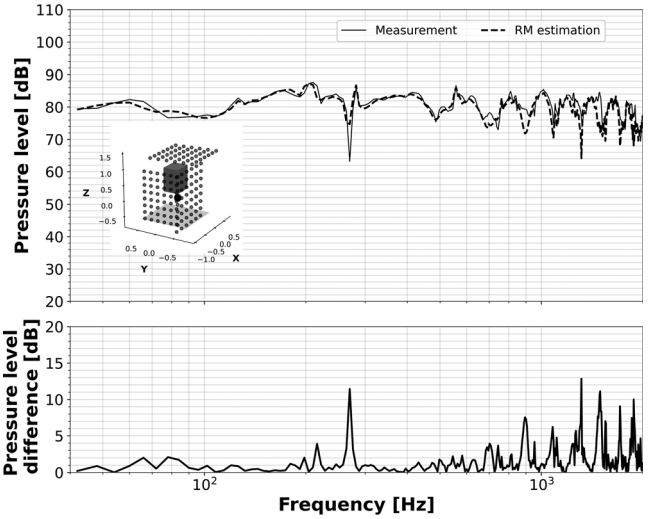

FIG. 18. (Upper graph) Frequency response at the point depicted by • for the "closed box" source. (Lower graph) Pressure level difference between measurement and RM method reconstruction.

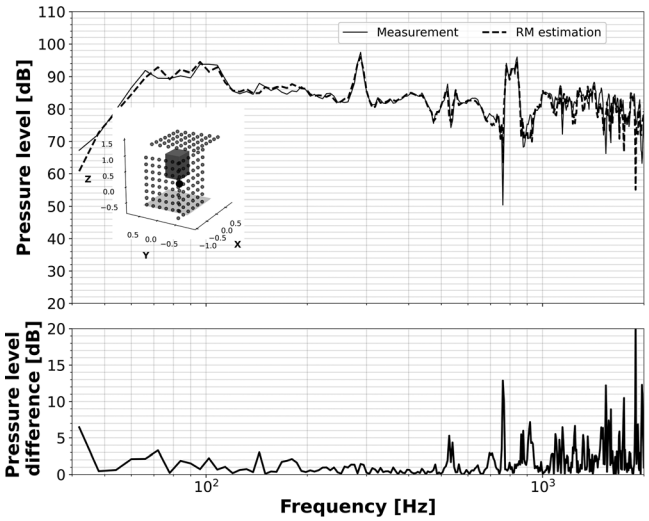

FIG. 19. (Upper graph) Frequency response at the point depicted by • for the "complex box" source. (Lower graph) Pressure level difference between measurement and RM method reconstruction.

box" source: discrepancy peaks at 220, 280, and 550 Hz coincide with the pressure level deviation peaks of Fig. 15. Nevertheless, it can be noted that the pressure reconstruction remains rather accurate (within ± 2 dB) over almost the whole frequency range.

Figures 18 and 19 represent the pressure reconstruction for the "closed box" and "complex box" sources at the point $[-0.9, -0.505, 0.37]$ m. This point is at a more or less equal distance from the upper loudspeaker and the floor. The RM pressure reconstruction sticks to the measurement within ± 2 dB over almost all of the frequency band range from 30 Hz to 1 kHz. The peaks of the difference between measurement and estimation are mostly related to the drops of pressure levels in the system response at this position. It can be noticed that, globally, the pressure field is correctly reconstructed, except for some points showing drops in pressure level.

Figure 20 presents an overview of the pressure reconstruction at all others P_e around the "complex source." Three maps at 762, 768, and 774 Hz show the pressure level differences between measurements and RM estimates. These frequencies are chosen in order to capture the dip at 770 Hz seen on Fig. 19. Once again, we note a quite small difference (<3 dB) between the measurements at all P_e and the pressure reconstruction with the RM technique. The difference only increases at specific locations corresponding to pressure level dips.

V. CONCLUSION AND FUTURE WORK

The present work studied the possibility to reconstruct the pressure generated in the far field by a complex source, using RMs computed over its surface. The RMs used in this work were calculated using a perfectly rigid radiation body.

Simulations and measurement tests were carried out for two systems of similar size: a closed box system with a body admittance close to that used for the RM calculation and a "worst case" source, including non-rigid walls, openings, and complex vibration patterns. In order to allow comparison with real measurements, noise was added to the simulated data.

Very good results have been obtained for both simulations and actual measurements. The difference between the estimated far-field pressure and the measured one remains within $2-3$ dB almost over all the frequency range. This difference increases on the system response minima, for which the chosen RM combination is not appropriate, as it favors directions where the pressure field is efficiently radiated.

Furthermore, for the actual measurements, correct results up to 2 kHz were obtained using a mesh with 70 mm side length elements. This extends considerably the rule of thumb of 6 elements per wavelength commonly used in BEMs: indeed, about 1 element per wavelength seems sufficient. This result probably comes from the truncation of the RM series to the first (most radiating) terms, which exhibit smooth patterns, so the required mesh does not need to represent the actual vibration field or geometrical details of the source body. The possibility to use very rough and approximate mesh has also been investigated and has led to a significant reduction in the calculation time for radiation modes,

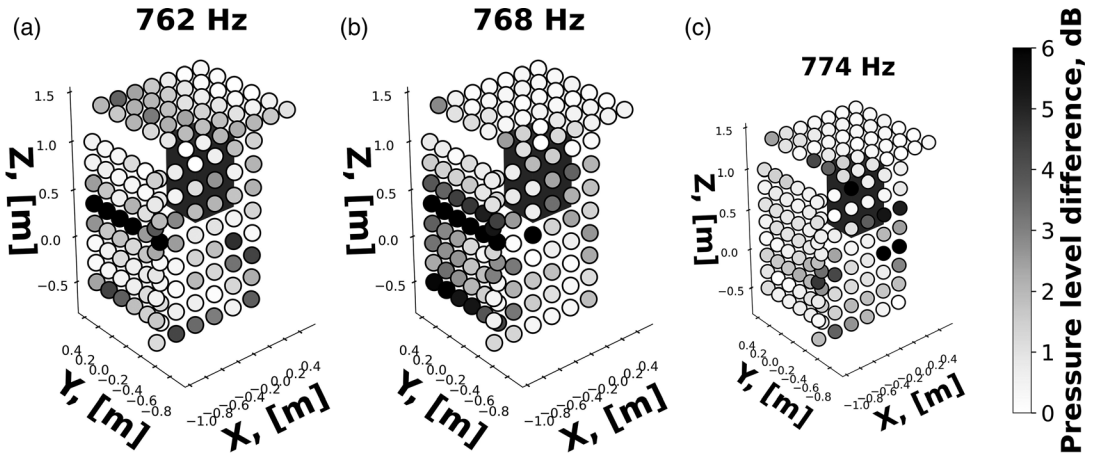

FIG. 20. Complex source cartography: 762 Hz (a), 768 Hz (b), and 774 Hz (c).

although with a reduction in the maximum frequency of use for the coarsest meshes. Indeed, decreasing of the number of elements in the mesh by 5 times decreases the computation time by 85 times.

The robustness of the RM technique to temperature variations was also investigated. Small temperature differences between measurements will cause very small estimation inaccuracy. As a result, it can be expected that RMs computed for a given temperature may be used for the pressure estimation at a different temperature.

Future work is still needed to improve the RM method: A better selection of the RM subset could be carried out to favor sparsity (thus reducing the computing time) or to allow for a better reconstruction of the dips in the radiation pattern. Another potential improvement would be the possibility to use the RMs calculated on a surface that does not exactly match the real shape of the tested object, thus simplifying the computer-aided design (CAD) modeling phase. As the RM method can reconstruct both acoustic pressure and velocity quantities, it could be used to extrapolate the intensity field, allowing virtual intensity mapping. More complex sources, with several incoherent radiated components, should then be tested. This might require a principal component analysis (PCA) step coupled to the RM method.

AUTHOR DECLARATIONS

Conflict of Interest

The authors have no conflicts to disclose.

DATA AVAILABILITY

The data that support the findings of this study are available from the corresponding author upon reasonable request.

[1]ISO-3741, "Acoustics. Determination of sound power levels and sound energy levels of noise sources using sound pressure. Precision methods for reverberation test rooms" (International Organization for Standardization, Geneva, Switzerland, 2010).
[2]ISO-3745, "Acoustics. Determination of sound power levels and sound energy levels of noise sources using sound pressure. Precision methods for anechoic rooms and hemi-anechoic rooms" (International Organization for Standardization, Geneva, Switzerland, 2012).
[3]ISO-11201, "Acoustics. Noise emitted by machinery and equipment. Determination of emission sound pressure levels at a work station and at other specified positions in an essentially free field over a reflecting plane with negligible environmental corrections" (International Organization for Standardization, Geneva, Switzerland, 2010).
[4]IEC-60268-5, "Sound system equipment. Part 5. Loudspeakers" (International Electrotechnical Commission, Geneva, Switzerland, 2007).
[5]ISO-9614-1, "Acoustics. Determination of sound power levels of noise sources using sound intensity. Part 1. Measurement at discrete points" (International Organization for Standardization, Geneva, Switzerland, 1993).
[6]M. Melon, C. Langrenne, D. Rousseau, and P. Herzog, "Comparison of four subwoofer measurement techniques," J. Audio. Eng. Soc. **55**(12), 1077–1091 (2007).
[7]C. J. Struck and S. F. Temme, "Simulated free field measurements," J. Audio Eng. Soc. **42**(6), 467–482 (1994).
[8]ISO-3746, "Acoustics. Determination of sound power levels and sound energy levels of noise sources using sound pressure. Survey method using an enveloping measurement surface over a reflecting plane" (International Organization for Standardization, Geneva, Switzerland, 2010).
[9]E. G. Williams, J. D. Maynard, and E. Skudrzyk, "Sound source reconstructions using a microphone array," J. Acoust. Soc. Am. **68**(1), 340–344 (1980).
[10]P. R. Stepanishen and H. Chen, "Nearfield pressures and surface intensity for cylindrical vibrators," J. Acoust. Soc. Am. **76**(3), 942–948 (1984).
[11]L. A. Devries and J. S. Bolton, "Acoustical holography in spherical coordinates for noise source identification," J. Acoust. Soc. Am. **95**(5), 2921 (1994).
[12]E. G. Williams, *Fourier Acoustics: Sound Radiation and Nearfield Acoustical Holography* (Academic Press, San Diego, 1999).
[13]J. Hald, "Basic theory and properties of statistically optimized near-field acoustical holography," J. Acoust. Soc. Am. **125**(4), 2105–2120 (2009).
[14]E. Fernandez-Grande, "Four decades of near-field acoustic holography," J. Acoust. Soc. Am. **152**(1), R1–R2 (2022).
[15]B. K. Gardner and R. J. Bernhard, "A noise source identification technique using an inverse Helmholtz integral equation method," J. Vib. Acoust. Stress Rel. Des. **110**(1), 84–90 (1988).
[16]W. Veronesi and J. Maynard, "Digital holographic reconstruction of sources with arbitrary shaped surfaces," J. Acoust. Soc. Am. **85**(2), 588–598 (1989).
[17]M. R. Bai, "Application of BEM (boundary element method)-based acoustic holography to radiation analysis of sound sources with arbitrarily shaped geometries," J. Acoust. Soc. Am. **92**(1), 533–549 (1992).
[18]C.-X. Bi, Y. Liu, Y.-B. Zhang, and L. Xu, "Sound field reconstruction using inverse boundary element method and sparse regularization," J. Acoust. Soc. Am. **145**(5), 3154–3162 (2019).
[19]Z.-W. Luo, D. Fernandez Comesana, C.-J. Zheng, and C.-X. Bi, "A free field recovery technique based on the boundary element method and three-dimensional scanning measurements," J. Acoust. Soc. Am. **150**(5), 3929–3948 (2021).
[20]M. Aucejo, N. Totaro, and J.-L. Guyader, "Identification of source velocities on 3D structures in non-anechoic environments: Theoretical background and experimental validation of the inverse patch transfer functions method," J. Sound Vib. **329**(18), 3691–3708 (2010).
[21]M. R. Bai, C.-C. Chen, and J.-H. Lin, "On optimal retreat distance for the equivalent source method-based nearfield acoustical holography," J. Acoust. Soc. Am. **129**(3), 1407–1416 (2011).
[22]V. Isakov and S. F. Wu, "On theory and application of the Helmholtz equation least squares method in inverse acoustics," Inverse Probl. **18**(4), 1147–1159 (2002).
[23]T. Semenova and S. F. Wu, "On the choice of expansion functions in the Helmholtz equation least-squares method," J. Acoust. Soc. Am. **117**(2), 701–710 (2005).
[24]S. F. Wu, "Methods for reconstructing acoustic quantities based on acoustic pressure measurements," J. Acoust. Soc. Am. **124**(5), 2680–2697 (2008).
[25]S. F. Wu, *The Helmholtz Equation Least Squares Method* (Springer, New York, 2015).
[26]C. Langrenne, M. Melon, and A. Garcia, "Boundary element method for the acoustic characterization of a machine in bounded noisy environment," J. Acoust. Soc. Am. **121**(5), 2750–2757 (2007).
[27]M. Melon, C. Langrenne, P. Herzog, and A. Garcia, "Evaluation of a method for the measurement of subwoofers in usual rooms," J. Acoust. Soc. Am. **127**(1), 256–263 (2010).
[28]C. Langrenne and A. Garcia, "Vector intensity reconstruction using the data completion method," J. Acoust. Soc. Am. **133**(4), 2198–2207 (2013).
[29]W. Lin, S. Li, S. Liu, H. Gao, J. Gao, and Y. Liu, "An improved method for recovering the acoustic characteristics of a target sound source sitting on plane by boundary element method," Appl. Acoust. **165**, 107316 (2020).
[30]D. Zhou, H. Lu, D. M. McFarland, and Y. Xiao, "Reconstruction of acoustic radiation of a vibrating structure located in a half-space bounded by a passive surface with finite acoustic impedance," J. Theor. Comp. Acoust. **28**(4), 2050019 (2020).
[31]H. Gao, Q. Zhu, S. Liu, P. Xing, and G. Li, "The formulations based on the indirect boundary element method for the acoustic characterization of an arbitrarily shaped source in a bounded noisy environment," Eng. Anal. Boundary Elem. **138**, 65–82 (2022).
[32]J. Hwang and S. Chang, "A retracted boundary integral equation for exterior acoustic problem with unique solution for all wave numbers," J. Acoust. Soc. Am. **90**(2), 1167–1180 (1991).

[33]L. Zhang, J. Wang, D. Yang, B. Hu, and D. Wu, "Optimization of the equivalent source configuration for the equivalent source method," J. Mar. Sci. Eng. **9**(8), 807 (2021).
[34]P. Herzog, R. Guillermin, P. Lorin, and V. Chritin, "Identification of a vibration pattern from pressure measurements and radiation modes," in *EuroNoise*, Maastricht, Netherlands (June 1–3, 2015) (European Acoustics Association, Madrid, Spain).
[35]M. Sanalatii, P. Herzog, M. Melon, R. Guillermin, J.-C. L. Roux, and N. Poulain, "Measurement of the frequency and angular responses of loudspeaker systems using radiation modes," in *Audio Engineering Society Convention 141*, Los Angeles, CA (September 29–October 2, 2016) (Audio Engineering Society, New York, 2016), preprint 9615.
[36]M. Sanalatii, L. Vindrola, C. Vasseur, P. Herzog, M. Melon, R. Guillermin, N. Poulain, and J.-C. L. Roux, "Assessment of the radiation mode method for *in situ* measurements of loudspeaker systems," in *The 142nd Audio Engineering Society Convention*, Berlin, Germany (May 20–23, 2017) (Audio Engineering Society, New York, 2017), preprint 9725.
[37]M. Sanalatii, P. Herzog, R. Guillermin, M. Melon, N. Poulain, and J.-C. L. Roux, "Estimation of loudspeaker frequency response and directivity using the radiation-mode method," J. Audio Eng. Soc. **67**(3), 101–115 (2019).
[38]G. V. Borgiotti, "The power radiated by a vibrating body in an acoustic fluid and its determination from boundary measurements," J. Acoust. Soc. Am. **88**(4), 1884–1893 (1990).
[39]A. Sarkissian, "Acoustic radiation from finite structures," J. Acoust. Soc. Am. **90**(1), 574–578 (1991).
[40]S.-C. Kang and J.-G. Ih, "Use of nonsingular boundary integral formulation for reducing errors due to near-field measurements in the boundary element method based near-field acoustic holography," J. Acoust. Soc. Am. **109**(4), 1320–1328 (2001).
[41]S. Marburg and B. Nolte, *Computational Acoustics of Noise Propagation in Fluids—Finite and Boundary Element Methods* (Springer, Berlin, 2008).
[42]S. Kirkup and J. Yazdani, "A gentle introduction to the boundary element method in Matlab/Freemat," in *Proceedings of the 10th WSEAS International Conference on Mathematical Methods, Computational Techniques, Non-Linear Systems, Intelligent Systems*, Corfu, Greece (WSEAS, Athens, Greece, 2008), pp. 46–52.
[43]C. Langrenne, A. Garcia, and M. Bonnet, "Solving the hypersingular boundary integral equation for the Burton and Miller formulation," J. Acoust. Soc. Am. **138**(5), 3332–3340 (2015).
[44]P.-T. Chen and J. H. Ginsberg, "Complex power, reciprocity, and radiation modes for submerged bodies," J. Acoust. Soc. Am. **98**(6), 3343–3351 (1995).
[45]P. Herzog and O. Schevin, "Estimation du degré de complexité d'un modèle de source vibrante" ("Estimation of the degree of complexity and the mode of source vibrancy"), in *Actes du 6ème Congrès Français D'Acoustique* (*Proceedings of the 6th French Congress Acoustics*), Lille, France (April 8–11, 2002) (Société Française d'Acoustique, Paris, France), abstract 075.
[46]G. H. Golub and C. F. V. Loan, *Matrix Computations* (John Hopkins University Press, Baltimore, 2013).
[47]S. M. Kirkup, *The Boundary Element Method in Acoustics* (Integrated Sound Software, Todmorden, UK, 2007).